

Neural network solvers for parametrized elasticity problems that conserve linear and angular momentum

Wietse M. Boon^a, Nicola R. Franco^b, Alessio Fumagalli^b

^aNORCE Norwegian Research Centre, Nygårdsgaten 112, Bergen, 5008, Norway

^bMOX Laboratory, Department of Mathematics, Politecnico di Milano, Piazza Leonardo da Vinci, Milan, 20133, Italy

Abstract

We consider a mixed formulation of parametrized elasticity problems in terms of stress, displacement, and rotation. The latter two variables act as Lagrange multipliers to enforce conservation of linear and angular momentum. Due to the saddle-point structure, the resulting system is computationally demanding to solve directly, and we therefore propose an efficient solution strategy based on a decomposition of the stress variable. First, a triangular system is solved to obtain a stress field that balances the body and boundary forces. Second, a trained neural network is employed to provide a correction without affecting the conservation equations. The displacement and rotation can be obtained by post-processing, if necessary. The potential of the approach is highlighted by three numerical test cases, including a non-linear model.

Keywords: parametrized PDEs, neural network solvers, momentum conservation, weak symmetry

2020 MSC: 65N30, 74G15, 68T07

1. Introduction

The development of reliable numerical solution strategies is crucial to accurately model and predict the behavior of elastic materials in engineering applications. However, the computational burden of solving the elasticity equations becomes prohibitive in many-query scenarios where the PDE needs to be solved repeatedly for different system configurations, including changes in the material laws, problem parameters, or boundary conditions. Instead, a common strategy is to replace expensive numerical simulations with a more efficient surrogate, known as a Reduced Order Model (ROM) [17, 24]. In this work, we focus on data-driven, non-intrusive ROMs using Deep Learning techniques, which have shown promising potential [21, 8, 11].

Because these approaches are entirely data-driven, they often produce solutions that violate underlying physical principles such as the conservation of mass, momentum, or energy. We herein adopt the viewpoint that, while some error in constitutive laws are tolerable, physical conservation laws need to be satisfied precisely.

A variety of deep-learning methods have been developed to ensure conservation laws in PDE modeling. Physics-Informed Neural Networks [25, 8] enforce these constraints through the loss function. However, this approach often proves insufficient as the constraints are not guaranteed to be satisfied exactly [16]. In contrast, exact constraint-preserving networks are explored in [4, 26], where the authors studied the incorporation of supplementary information into neural networks for modeling dynamical systems. In [28], a data-driven exterior calculus is introduced to produce structure-preserving ROMs that adhere to physical laws. Finally, [3] proposed enforcing analytical constraints by mapping the solution onto the kernel of the

constraint operator. In this work, we follow a similar strategy and develop such projection operators explicitly.

In [6, 5], a strategy is proposed to construct solvers that guarantee mass conservation for flow problems. This work effectively extends those ideas to the case of parameterized elasticity problems. We focus on a mixed formulation of the elasticity equation that explicitly includes the linear and angular momentum balance equations. We discretize these equations by employing the low-order mixed finite element triplet from [1] to model the stress, displacement, and rotation variables.

Our method involves decomposing the stress tensor into two parts: a particular solution that balances the body and boundary forces, and a homogeneous correction that conserves linear and angular momentum locally. We approximate these components separately. For the particular solution, we propose an efficient solution procedure based on a spanning tree in the mesh. For the remainder, we consider suitable neural network architectures combined with a kernel projector, which ensures that the output remains within the null space of the constraint operator. Through this procedure, we ensure that the stress field satisfies the conservation equations up to machine precision. Finally, the spanning tree can be employed again to efficiently post-process the displacement and rotation fields.

The paper is structured as follows. In Section 2, we introduce the elastic models compatible with our approach, as well as the mixed finite element discretization. Section 3 is dedicated to the construction of a spanning tree solver, an ingredient of fundamental importance for our construction. Next, the relevant background and preliminaries on deep learning algorithms are presented in Section 4. Section 5 combines the spanning tree and deep learning techniques to form our reduced order models. Numerical experiments, designed to compare performance across problems of increasing complexity, are discussed in Section 6. Finally, concluding remarks are given in Section 7 and we provide additional details concerning Proper Orthogonal Decomposition and the used neural networks in Appendix A.

2. Model problems

Let $\Omega \in \mathbb{R}^d$ with $d = 2, 3$ be a Lipschitz, polytopal domain and let its boundary be disjointly partitioned as $\partial\Omega = \partial_u\Omega \cup \partial_\sigma\Omega$ with $|\partial_u\Omega| > 0$. We consider a mixed formulation of elasticity problems in which the stress field is a primary variable. This allows us to explicitly impose the balance of linear and angular momentum as equations in the system. We thus consider the problem unknowns

$$\sigma : \Omega \rightarrow \mathbb{R}^{d \times d}, \quad u : \Omega \rightarrow \mathbb{R}^d, \quad r : \Omega \rightarrow \mathbb{R}^{\binom{d}{2}}. \quad (2.1)$$

in which σ denotes the Cauchy stress tensor, u is the displacement, and r is a variable commonly referred to as the *rotation*. Note that r is a scalar variable in 2D and a vector field in 3D. The rotation acts as a Lagrange multiplier to enforce symmetry of σ through the operator $\text{asym} : \mathbb{R}^{d \times d} \rightarrow \mathbb{R}^{\binom{d}{2}}$. This operator, and its adjoint asym^* , are given by:

$$\text{asym } \sigma = \begin{bmatrix} \sigma_{32} - \sigma_{23} \\ \sigma_{13} - \sigma_{31} \\ \sigma_{21} - \sigma_{12} \end{bmatrix}, \quad \text{asym}^* r = \begin{bmatrix} 0 & -r_3 & r_2 \\ r_3 & 0 & -r_1 \\ -r_2 & r_1 & 0 \end{bmatrix}, \quad d = 3,$$

$$\text{asym } \sigma = \sigma_{21} - \sigma_{12}, \quad \text{asym}^* r = \begin{bmatrix} 0 & -r \\ r & 0 \end{bmatrix}, \quad d = 2.$$

We are interested in elasticity problems of the form: find (σ, u, r) such that

$$A\sigma - \nabla u - \text{asym}^* r = 0, \quad (2.2a)$$

$$-\nabla \cdot \sigma = f_u, \quad (2.2b)$$

$$\text{asym} \sigma = 0, \quad (2.2c)$$

on Ω , subject to the boundary conditions

$$u = g_u \text{ on } \partial_u \Omega, \quad \nu \cdot \sigma = 0 \text{ on } \partial_\sigma \Omega. \quad (2.2d)$$

Here, f_u is a given body force, g_u prescribes the displacement on the boundary $\partial_u \Omega$, and ν is the outward unit normal of $\partial \Omega$. For clarity, we moreover note that ∇u denotes the gradient of the displacement and $\nabla \cdot \sigma$ refers to the row-wise divergence on the Cauchy stress.

We briefly elaborate on the physical meaning of the equations of (2.2). First, the operator $A : \mathbb{R}^{d \times d} \rightarrow \mathbb{R}^{d \times d}$ in (2.2a) is the (possibly non-linear), stress-strain relationship. Depending on the material properties, different laws can be considered, resulting in different choices, and parametrizations, of A . We report two examples below.

Example 2.1 (Hooke's law). *In the case of linearized elasticity and an isotropic, homogeneous material, the stress-strain relation is given by*

$$A\sigma := \frac{1}{2\mu} \left(\sigma - \frac{\lambda}{2\mu + d\lambda} \text{Tr}(\sigma)I \right), \quad (2.3)$$

in which μ and λ are the Lamé parameters, Tr denotes the matrix trace and I is the identity tensor. The inverse of A yields the recognizable expression:

$$A^{-1}\varepsilon = 2\mu\varepsilon + \lambda \text{Tr}(\varepsilon)I.$$

Example 2.2 (Hencky-von Mises). *As investigated in [13, 9], the Hencky-von Mises model defines the stress-strain relationship A as in (2.3), but the Lamé parameters are modeled as functions of the deviatoric strain, i.e.*

$$\mu = \mu(\|\text{dev}(\varepsilon)\|), \quad \lambda = \lambda(\|\text{dev}(\varepsilon)\|).$$

Here, $\varepsilon = \frac{1}{2}(\nabla u + (\nabla u)^\top)$ is the linearized strain tensor, $\|\cdot\|$ denotes the Frobenius norm, and dev denotes the deviator $\text{dev}(\tau) := \tau - \frac{1}{d} \text{Tr}(\tau)$. We emphasize that the operator A is non-linear in this case.

The conservation laws are given by (2.2b) and (2.2c). The first conservation law describes the balance of linear momentum. By choosing appropriate finite element spaces (cf. Section 2.1), we will impose this law strongly and pointwise in Ω .

The second conservation law is the balance of angular momentum which, under the assumption of linear momentum conservation, is equivalent to imposing the symmetry of the Cauchy stress tensor, i.e. (2.2c). Due to the difficulties in constructing stable mixed finite elements that exactly satisfy this constraint, we herein follow [1] and impose the symmetry constraint weakly.

We emphasize that we only consider models that feature linear conservation laws (2.2b) and (2.2c), while allowing for non-linearities in the constitutive law (2.2a).

Remark 2.3 (Hyperelasticity). *In the case of hyperelasticity, the infinitesimal strain ε is replaced by the Lagrangian Green strain $E := \varepsilon + \frac{1}{2}(\nabla u)^\top(\nabla u)$. Additionally, the second Piola-Kirchhoff stress tensor is given by*

$$S = 2\mu E + \lambda \text{Tr}(E)I,$$

The momentum balance and symmetry constraints are now given by

$$-\nabla \cdot (FS) = f_u, \quad \text{asym } S = 0,$$

in which F is the deformation gradient. Note that the equation describing linear momentum has become non-linear. Changing variables to the first Piola-Kirchhoff stress tensor $P := FS$ does not improve matters because this would introduce a non-linearity in the symmetry constraint instead. The approach from [5], which we follow herein, is only valid for linearly constrained systems and thus hyperelasticity falls outside the scope of this work.

As mentioned in the introduction, we aim to construct efficient numerical solvers that, given a problem of interest, can rapidly produce multiple simulations for varying parameters (e.g. different values of the Lamé parameters μ, λ , perturbations in the body force f_u , or changes in the boundary conditions g_u for the displacement). Specifically, we are interested in surrogate models based on neural networks that produce accurate simulations after training on a set of pre-computed solutions $\{(\sigma_i, u_i, r_i)\}_i$, obtained for various configurations of the system.

We will only employ neural networks in the solving stages of the problem. This means that we will specify the finite element basis beforehand and propose a solver to produce the coefficients. We therefore dedicate the next subsection to a brief explanation of the chosen finite element spaces.

2.1. A mixed finite element discretization

Let the mesh Ω_h be a shape-regular, simplicial tessellation of Ω . For the discretization of (2.2), we will consider the finite element triplet of lowest order proposed in [2, 1]. These spaces are given by (tuples of) the Brezzi-Douglas-Marini element \mathbb{BDM}_1 and the piecewise constants \mathbb{P}_0 on Ω_h :

$$\Sigma_h := \{\sigma_h \in \mathbb{BDM}_1^d(\Omega_h) : \nu \cdot \sigma = 0 \text{ on } \partial_\sigma \Omega\}, \quad (2.4a)$$

$$U_h := \mathbb{P}_0^d(\Omega_h), \quad R_h := \mathbb{P}_0^{\binom{d}{2}}(\Omega_h) \quad (2.4b)$$

The finite element problem then becomes: find $(\sigma_h, u_h, r_h) \in \Sigma_h \times U_h \times R_h$ such that

$$\langle A\sigma_h, \tilde{\sigma}_h \rangle_\Omega + \langle u_h, \nabla \cdot \tilde{\sigma}_h \rangle_\Omega - \langle r_h, \text{asym } \tilde{\sigma}_h \rangle_\Omega = \langle g_u, \nu \cdot \tilde{\sigma}_h \rangle_{\partial_u \Omega} \quad (2.5a)$$

$$-\langle \nabla \cdot \sigma_h, \tilde{u}_h \rangle_\Omega = \langle f_u, \tilde{u}_h \rangle_\Omega \quad (2.5b)$$

$$\langle \text{asym } \sigma_h, \tilde{r}_h \rangle_\Omega = 0, \quad (2.5c)$$

for all test functions $(\tilde{\sigma}_h, \tilde{u}_h, \tilde{r}_h) \in \Sigma_h \times U_h \times R_h$. Here $\langle \phi, \psi \rangle_\Omega := \int_\Omega \phi(x)\psi(x)dx$ and $\langle \phi, \psi \rangle_{\partial_u \Omega} := \int_{\partial_u \Omega} \phi(s)\psi(s)ds$ denote the relevant L^2 inner products. It was shown in [1] that, assuming lower and upper bounds on A , Problem (2.5) admits a unique solution that is bounded in the following norms:

$$\|\sigma_h\|_{\Sigma_h}^2 := \|\sigma_h\|_{L^2(\Omega)}^2 + \|\nabla \cdot \sigma_h\|_{L^2(\Omega)}^2, \quad (2.6a)$$

$$\begin{aligned} \|(u_h, r_h)\|_{X_h}^2 &:= \|u_h\|_{U_h}^2 + \|r_h\|_{R_h}^2 \\ &:= \|u_h\|_{L^2(\Omega)}^2 + \|r_h\|_{L^2(\Omega)}^2. \end{aligned} \quad (2.6b)$$

When A is linear, e.g. as in Example 2.1, problem (2.5) is a linear system in the unknowns (σ_h, u_h, r_h) that can be addressed with a direct solver. However, if A is non-linear, then iterative solvers are required, and we propose a specific scheme in the following example.

Example 2.4 (Iterative solver for the Hencky-von Mises model). *Example 2.2 assumes that the Lamé parameters depend on the deviatoric strain. In our discrete formulation, we do not immediately have access to the strain (nor its deviator) since the displacement u_h is only given as a piecewise constant. However, we can retrieve the deviatoric strain by applying the deviator on the stress-strain relationship:*

$$\text{dev}(\sigma) = 2\mu \text{dev}(\varepsilon) + \lambda \text{Tr}(\varepsilon) \text{dev}(I) = 2\mu \text{dev}(\varepsilon),$$

and thus, $\|\text{dev}(\sigma)\| = 2\mu\|\text{dev}(\varepsilon)\|$. Using this observation, we will solve (2.5) using the following iterative scheme:

1. Set $i = 0$ and compute an initial guess $(\sigma_0, u_0, r_0) \in \Sigma_h \times U_h \times R_h$, e.g. by solving (2.5) with constant Lamé parameters.
2. Evaluate σ_i at the cell centers and compute the norm of its deviator.
3. In each cell, solve the following non-linear equation for $0 \leq \zeta \in \mathbb{R}$:

$$2\mu(\zeta)\zeta = \|\text{dev}(\sigma_i)\|.$$

4. Evaluate $\mu = \mu(\zeta)$, $\lambda = \lambda(\zeta)$, then solve (2.5) to obtain $(\sigma_{i+1}, u_{i+1}, r_{i+1})$. Increment $i \leftarrow i + 1$.
5. Iterate steps 2-4 until convergence.

3. A spanning tree solver for the stress

We now leverage the mathematical structure of the Full-Order Model (FOM) discretization (2.5) to derive an efficient numerical solver that, despite operating at FOM level, handles the conservation of linear and angular momentum in linear time. This will be a fundamental ingredient for our construction of reduced order models in Section 5.

To start, we introduce the following short-hand notation for the *constraint operator* $B : \Sigma_h \rightarrow U'_h \times R'_h$ and the functional $f \in U'_h \times R'_h$:

$$\begin{aligned} \langle B\sigma_h, (\tilde{u}_h, \tilde{r}_h) \rangle &:= -\langle \nabla \cdot \sigma_h, \tilde{u}_h \rangle_\Omega + \langle \text{asym } \sigma_h, \tilde{r}_h \rangle_\Omega, \\ \langle f, (\tilde{u}_h, \tilde{r}_h) \rangle &:= \langle f_u, \tilde{u}_h \rangle_\Omega \end{aligned}$$

in which U'_h and R'_h are the dual spaces of U_h and R_h , respectively, and the angled brackets on the left-hand side indicate duality pairings. The conservation laws (2.2b)-(2.2c) can then be expressed as

$$B\sigma = f, \tag{3.1}$$

For parametric problems, we adopt a subscript f_μ to indicate the dependency on a set of parameters collected in the vector μ . We emphasize that the operator B is linear and independent of μ .

As discussed in [5], we can handle linear constraints such as (3.1) by constructing a right-inverse of the constraint operator. In particular, we construct an operator S_I that, for any given $f \in U'_h \times R'_h$ produces a $S_I f \in \Sigma_h$ such that

$$BS_I f = f.$$

To construct $S_I f$ for a given $f \in U'_h \times R'_h$, we first consider the surjectivity of the operator B . For that, we recall the following result.

Lemma 3.1. *The discrete spaces given by (2.4a) satisfy the following condition:*

$$\inf_{(u_h, r_h) \in U_h \times R_h} \sup_{\sigma_h \in \Sigma_h} \frac{\langle B\sigma_h, (u_h, r_h) \rangle}{\|\sigma_h\|_{\Sigma_h} \|(u_h, r_h)\|_{X_h}} \geq C > 0$$

with C independent of the mesh size h .

Proof. See [1, Thm. 7.1]. □

The inf-sup condition of Lemma 3.1 implies that if $\langle B\sigma_h, (u_h, r_h) \rangle = 0$ for all $\sigma_h \in \Sigma_h$, then $(u_h, r_h) = (0, 0)$. In other words, B is surjective.

We now briefly consider the edge case where an element ω borders multiple boundaries on which essential boundary conditions are imposed, such that only one of its facets, γ , contains degrees of freedom in the space Σ_h . Since the proof of Lemma 3.1 covers this case, this means that the operator B restricted to this single facet γ remains surjective on the space restricted to ω . In turn, we may construct S_{lf} by moving through the grid one facet and cell at a time. We do this by constructing a *spanning tree* as follows.

We start by considering the dual grid of Ω_h as a graph. In particular, we construct a graph \mathcal{G} by assigning a node to each cell $\omega \in \Omega_h$ and we connect two nodes with an edge if the corresponding cells share a facet. Next, we choose a cell ω_0 that borders the boundary $\partial_u \Omega$ and an adjacent facet γ_0 on that boundary. We then construct a spanning tree \mathcal{T} of the graph \mathcal{G} rooted at the node corresponding to ω_0 . An example is illustrated in Figure 1(left). For readers unfamiliar with the concept, we recall that a spanning tree is a connected subgraph that: i) contains all the vertices of the original graph, ii) has no cycles. These structures are often employed to re-organize data on graphs. For an example in the context of finite elements, see [10].

Remark 3.2 (Multiple roots). *Alternatively, we may choose multiple roots near the boundary to construct multiple trees that, together, form a spanning forest that reaches every cell in the grid exactly once. An example is illustrated in Figure 1(right).*

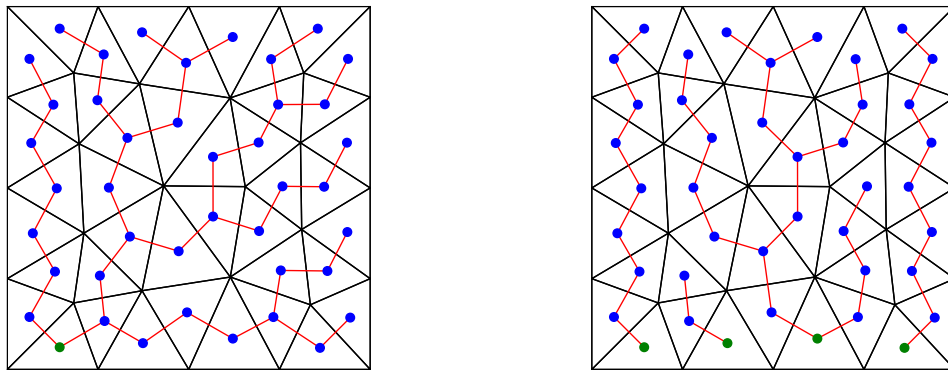


Figure 1: Example of spanning trees for a two-dimensional grid, on the left with single root (green dot) and on the right with multiple roots. Each root is associated to a facet on the boundary on which a displacement boundary condition is imposed.

The edges of the tree \mathcal{T} correspond to a subset of facets in the grid Ω_h and, together with the root facet γ_0 , we refer to this set as $\mathcal{F}_{\mathcal{T}}$. Note that this set contains as many facets as there are cells in the grid. This is due to the fact that the number of nodes in a tree is one higher than its number of edges, and we have included the boundary facet in $\mathcal{F}_{\mathcal{T}}$.

We now combine the surjectivity of B with the spanning tree \mathcal{T} . In particular, we note that the degrees of freedom of \mathbb{BDM}_1^d on $\mathcal{F}_{\mathcal{T}}$ are sufficient to construct a right-inverse of B . However, on each facet, we have 9 degrees of freedom (4 in 2D) and 6 equations to fulfill per cell (3 in 2D). Indeed, the space \mathbb{BDM}_1^d contains more degrees of freedom than necessary for the surjectivity to hold. This was also observed in [1, Sec. 8] and, consequently, a reduced space was proposed, which we denote by \mathbb{AFW}^- . This space has 6 degrees of freedom per facet in 3D, respectively 3 in 2D, and therefore matches exactly the number of equations we need to satisfy. The explicit degrees of freedom can be found in [1, Sec. 8] and [2, Sec. 11.8].

As shown in [2, 1], the analogue of Lemma 3.1 holds in the reduced space, namely:

$$\inf_{(u_h, r_h) \in U_h \times R_h} \sup_{\sigma_h \in \mathbb{AFW}^-} \frac{\langle B\sigma_h, (u_h, r_h) \rangle}{\|\sigma_h\|_{\Sigma_h} \|(u_h, r_h)\|_{X_h}} \geq c > 0$$

Let now $\Pi : \mathbb{BDM}_1^d(\Omega_h) \rightarrow \mathbb{AFW}^-(\mathcal{F}_{\mathcal{T}})$ be the restriction onto those degrees of freedom of the reduced space that are on the facets of $\mathcal{F}_{\mathcal{T}}$. Its adjoint Π^* is then an inclusion operator into \mathbb{BDM}_1^d .

Following the same arguments as above, the operator $B\Pi^*$ is surjective as well. Let $B\Pi^T \in \mathbb{R}^{n \times n}$ be its matrix representation with $n = \dim(U_h) + \dim(R_h) = \dim(\mathbb{AFW}^-(\mathcal{F}_{\mathcal{T}})) = 6 \cdot n_{cells}$, respectively $3 \cdot n_{cells}$ in 2D. Since it is a square, surjective matrix, it is invertible, which allows us to define:

$$S_I := \Pi^*(B\Pi^*)^{-1}$$

It is easy to see that S_I is a right-inverse of B . This operator will be the key building block in our construction because it provides a weakly-symmetric stress field that balances the forces. In turn, we only need to provide a correction that lies in the kernel of B , for which we will use trained neural networks.

Remark 3.3. *The application of S_I involves solving a sparse linear system. Due to the underlying spanning tree structure, this linear system is equivalent to a triangular matrix. In particular, we may solve the equations relevant to the leaf nodes first, which decides the degrees of freedom on the adjacent face. We can then progress iteratively through the tree towards the root. Since there are only 6 equations per cell, this system can be solved in linear time with respect to the number of cells.*

We conclude this section by noting that S_I can be used to reconstruct the displacement and rotation variables. In particular, for given stress σ_h , we can use the adjoint $S_I^* : \Sigma'_h \rightarrow U_h \times R_h$ and (2.2a) to derive

$$(u_h, r_h) = (BS_I)^*(u_h, r_h) = S_I^*(B^*(u_h, r_h)) = S_I^*(A_h\sigma_h - g_h) \quad (3.2)$$

in which $A_h : \Sigma_h \rightarrow \Sigma'_h$ and $g_h \in \Sigma'_h$ are defined such that:

$$\langle A_h\sigma_h, \tilde{\sigma}_h \rangle := \langle A\sigma_h, \tilde{\sigma}_h \rangle_{\Omega}, \quad \langle g_h, \tilde{\sigma}_h \rangle := \langle g_u, \nu \cdot \tilde{\sigma}_h \rangle_{\partial_u \Omega}$$

Finally, recall that S_I involves solving a sparse and triangular system. The adjoint operator solves the transpose problem, which is also sparse and triangular, so the post-processing of the displacement and rotation can be done efficiently for given σ_h , A_h , and g_u .

4. Preliminaries on neural network based non-linear regression

In this section, we recall some fundamental concepts of deep learning, starting from the definition and training of classical neural network architectures. A brief overview of the POD-NN approach is also presented. Readers familiar with these concepts may skip this section and proceed to Section 5.

4.1. Black-box models: definition and training

Feed forward neural networks are computational units commonly employed for non-linear regression. At their core, neural networks are based on the composition of affine transformations and non-linear activations. We provide a rigorous definition for clarity.

Definition 4.1 (Layer). *Let $\rho : \mathbb{R} \rightarrow \mathbb{R}$ and let $m, n \in \mathbb{N}_+$. A map $L : \mathbb{R}^m \rightarrow \mathbb{R}^n$ is said to be a layer with activation function ρ if it can be expressed as*

$$L(y) = \rho(Wy + b),$$

for a suitable matrix $W \in \mathbb{R}^{n \times m}$, called *weight-matrix*, and a suitable vector $b \in \mathbb{R}^n$, called *bias vector*. Here, the action of the activation function ρ is intended component-wise, i.e. $\rho([w_1, \dots, w_m]^\top) := [\rho(w_1), \dots, \rho(w_m)]^\top$. If ρ is the identity, the layer is said to be *affine*.

Definition 4.2 (Feed forward neural network). *Let $\rho : \mathbb{R} \rightarrow \mathbb{R}$. A neural network with activation function ρ is any map $\Phi : \mathbb{R}^m \rightarrow \mathbb{R}^n$ that can be expressed as*

$$\Phi(v) = (L_k \circ \dots \circ L_0)(v), \quad (4.1)$$

where $L_k : \mathbb{R}^{n_k} \rightarrow \mathbb{R}^{n_{k+1}}$ is an affine layer, whereas $L_i : \mathbb{R}^{n_i} \rightarrow \mathbb{R}^{n_{i+1}}$ are all layers with activation function ρ . Here, $n_0 := m$.

To illustrate the use of neural network models for non-linear regression, let us assume we are given a map

$$\mathcal{F} : M \ni \boldsymbol{\mu} \mapsto \boldsymbol{y}_\mu \in \mathbb{R}^{N_h},$$

where $M \subset \mathbb{R}^p$ and \mathbb{R}^{N_h} denote the input and output spaces, respectively. In our case, $\boldsymbol{\mu}$ will be the vector of parameters parametrizing the elasticity problem whereas \boldsymbol{y}_μ is the vector containing the finite element coefficients of the stress field. Consequently, \mathcal{F} corresponds to the full-order model.

We are interested in learning \mathcal{F} , i.e., in finding a suitable neural network model that can approximate the map $\boldsymbol{\mu} \mapsto \boldsymbol{y}_\mu$. We assume that the reference model \mathcal{F} is at our disposal during the training phase. The classical procedure consists of three steps. First, the *sampling phase* consists of querying \mathcal{F} to construct a training set

$$\{\boldsymbol{\mu}_i, \boldsymbol{y}_{\boldsymbol{\mu}_i}\}_{i=1}^N \subset M \times \mathbb{R}^{N_h}.$$

The second step concerns the design of a suitable neural network architecture

$$\Phi : \mathbb{R}^p \rightarrow \mathbb{R}^{N_h}.$$

This corresponds to choosing the number of layers in (4.1), together with their input-output dimensions, without specifying their weight matrices and bias vectors: these are collected in a common list $\theta := (W_0, \mathbf{b}_0, \dots, W_k, \mathbf{b}_k)$ and regarded as tunable parameters. The final step is the so-called *training phase*, which ultimately consists in solving the following minimization problem

$$\theta_* := \operatorname{argmin}_\theta \frac{1}{N} \sum_{i=1}^N \|\boldsymbol{y}_{\boldsymbol{\mu}_i} - \Phi_\theta(\boldsymbol{\mu}_i)\|_Y^2. \quad (4.2)$$

Here, $\|\cdot\|_Y$ is a given norm defined over the output space \mathbb{R}^{N_h} . The right-hand-side of (4.2) is commonly known as *loss function*, here defined using the mean squared error metric. Once the training phase is completed, the non-linear regression model is obtained as $\Phi := \Phi_{\theta_*}$.

We mention that, in general, the training phase can be computationally challenging due to i) non-linearity and non-convexity of the loss function and ii) the large number of trainable parameters. To overcome this difficulty, several strategies have been developed. We highlight the so-called *POD-NN approach*, which has the advantage of simplifying the training phase when N_h is large. We provide a quick overview in the next subsection.

4.2. The POD-NN strategy

POD-NN is a technique combining Proper Orthogonal Decomposition (POD), a commonly used dimensionality reduction technique, and neural networks (NN). The approach was originally developed in the context of model order reduction [18]. More precisely, it was introduced as a data-driven alternative of the so-called reduced basis method [24]. In subsequent years it was re-discovered, and generalized, under different names, such as PCA-net and POD-DeepONet [22, 23]. From a purely practical point of view, however, the POD-NN approach can be regarded as an alternative training strategy applied to classical neural network regression.

To illustrate the idea, let $\Phi_\theta : \mathbb{R}^p \rightarrow \mathbb{R}^{N_h}$ be a trainable neural network architecture, where $\theta := (W_0, \mathbf{b}_0, \dots, W_k, \mathbf{b}_k)$ as before. Let $n \in \mathbb{N}_+$ be such that $W_k \in \mathbb{R}^{N_h \times n}$. We can highlight the presence of the last layer by re-writing the action of the neural network model as

$$\Phi_\theta(\boldsymbol{\mu}) = W_k \phi_{\tilde{\theta}}(\boldsymbol{\mu}) + \mathbf{b}_k,$$

where $\phi_{\tilde{\theta}} : \mathbb{R}^p \rightarrow \mathbb{R}^n$ is the submodule collecting all layers except for the last one, so that $\tilde{\theta} := (W_0, \mathbf{b}_0, \dots, W_{k-1}, \mathbf{b}_{k-1})$. Assume that $\mathbf{b}_k \equiv 0$. Then, it is straightforward to see that, for every $\boldsymbol{\mu} \in M$, the vector $\Phi_\theta(\boldsymbol{\mu}) \in \mathbb{R}^{N_h}$ lies in the subspace of \mathbb{R}^{N_h} spanned by the columns of W_k . In particular, if $V \in \mathbb{R}^{N_h \times n}$ is an orthonormal matrix spanning the same subspace of W_k , by optimality of orthogonal projections we have

$$\|\mathbf{y}_\boldsymbol{\mu} - \Phi_\theta(\boldsymbol{\mu})\| = \|\mathbf{y}_\boldsymbol{\mu} - W_k \phi_{\tilde{\theta}}(\boldsymbol{\mu})\| \leq \|\mathbf{y}_\boldsymbol{\mu} - VV^\top \mathbf{y}_\boldsymbol{\mu}\|$$

for all $\boldsymbol{\mu} \in M$. With this observation, the POD-NN approach proposes the following design and training strategy:

1. For a given tolerance $\epsilon > 0$, find a suitable $n \in \mathbb{N}_+$ and a corresponding matrix $V \in \mathbb{R}^{N_h \times n}$ such that

$$\frac{1}{N} \sum_{i=1}^N \|\mathbf{y}_{\boldsymbol{\mu}_i} - VV^\top \mathbf{y}_{\boldsymbol{\mu}_i}\|^2 < \epsilon^2. \quad (4.3)$$

In practice, this can be achieved by leveraging the POD algorithm, which is ultimately based on a truncated singular value decomposition. We refer the interested reader to Appendix A.

2. Introduce a trainable network $\phi_{\tilde{\theta}} : \mathbb{R}^p \rightarrow \mathbb{R}^n$ and train it according to the loss function

$$\mathcal{L}(\tilde{\theta}) := \frac{1}{N} \sum_{i=1}^N \|c_{\boldsymbol{\mu}_i} - \phi_{\tilde{\theta}}(\boldsymbol{\mu}_i)\|^2, \quad (4.4)$$

where $c_{\boldsymbol{\mu}} := V^\top \mathbf{y}_{\boldsymbol{\mu}}$ are the ideal coefficients over the POD basis.

3. Define $\Phi = \Phi_{\text{POD}}$ as $\Phi_{\text{POD}}(\boldsymbol{\mu}) := V\phi(\boldsymbol{\mu})$, where $\phi = \phi_{\tilde{\theta}_*}$ is the trained module.

For the sake of simplicity, we presented the POD-NN strategy using the ℓ^2 -norm $\|\cdot\|$ (Euclidean norm). However, the procedure can be adjusted to account for arbitrary norms $\|\cdot\|_Y$ satisfying the parallelogram rule, cf. Remark 4.3.

Remark 4.3. *One can easily adapt the construction in Section 4.2 to ensure optimality in any norm induced by an inner-product. Given such a norm $\|\cdot\|_Y$, let $D \in \mathbb{R}^{N_h \times N_h}$ be its Gramian matrix, so that $\|\mathbf{y}\|_Y^2 = \mathbf{y}^\top D \mathbf{y}$. Then, the POD-matrix V can be constructed to be $\|\cdot\|_Y$ -orthonormal, meaning that $V^\top D V = I_n$: cf. Appendix A.*

Alternatively, one may use the ℓ^2 -norm to construct \mathbf{V} , as in (4.3), but then re-introduce the norm $\|\cdot\|_Y$ at the latent level. Note that for $c_\mu := \mathbf{V}^\top y_\mu$, by the triangular inequality,

$$\begin{aligned} \|y_\mu - \Phi_\theta(\mu)\|_Y &\leq \|y_\mu - \mathbf{V}c_\mu\|_Y + \|\mathbf{V}c_\mu - \mathbf{V}\phi_{\bar{\theta}}(\mu)\|_Y = \\ &= \|y_\mu - \mathbf{V}c_\mu\|_Y + \|c_\mu - \phi_{\bar{\theta}}(\mu)\|_{\mathbb{D}^{1/2}\mathbf{V}}, \end{aligned}$$

where $\|\cdot\|_{\mathbb{D}^{1/2}\mathbf{V}}$ is the norm over \mathbb{R}^n defined via the relation

$$\|a\|_{\mathbb{D}^{1/2}\mathbf{V}}^2 = a^\top (\mathbf{V}^\top \mathbf{D} \mathbf{V}) a.$$

In particular, one can: i) choose n and construct \mathbf{V} via classical POD so that, a posteriori, $\|y_\mu - \mathbf{V}\mathbf{V}^\top y_\mu\|_Y$ is below a given tolerance, ii) train $\phi_{\bar{\theta}}$ by minimizing a weighted loss in which $\|\cdot\|_{\mathbb{D}^{1/2}\mathbf{V}}$ replaces the Euclidean norm in (4.4). In this work, this is the default implementation of the POD-NN strategy.

Remark 4.4. It can be shown that, regardless of the underlying norm, the POD-matrix is always expressible as linear combination of the training snapshots. Consequently,

$$\Phi_{\text{POD}}(\mu) \in \text{span}(\mathbf{V}) \subseteq \text{span}(\{y_{\mu_1}, \dots, y_{\mu_N}\}) \quad \forall \mu \in M.$$

In particular, POD-NN surrogates preserve homogeneous linear constraints. That is, if $Dy_\mu \equiv 0$ for some linear operator D and all $\mu \in M$, then $D\Phi_{\text{POD}} \equiv 0$. In particular, for any $\mu \in M$,

$$\Phi_{\text{POD}}(\mu) \in \text{span}(\{y_{\mu_i}\}_{i=1}^N) \subseteq \ker(D) \implies D\Phi_{\text{POD}}(\mu) = 0.$$

5. Learnable solvers that preserve linear and angular momentum

We now come to our main subject, which is the development of learnable solvers for parametrized PDEs with conservation properties. To this end, let $M \subset \mathbb{R}^p$ denote the parameter space. We consider elasticity problems of the form (2.2) where the operator A , the source term f_u and the boundary term g_u depend on a vector of p parameters, denoted as $\mu \in M$. We assume that for each $\mu \in M$ the problem is well posed. The FOM described in Section 2.1 defines a map

$$M \ni \mu \mapsto (\sigma_\mu, u_\mu, r_\mu) \in \Sigma_h \times U_h \times R_h. \quad (5.1)$$

Note that $\Sigma_h \times U_h \times R_h$ is independent of μ because we adopt the discretization from Section 2.1 for all parameter values.

Learnable solvers aim to approximate the parameter-to-solution map (5.1) by leveraging a set of pre-computed FOM solutions, called the *training set*, obtained by sampling N parameter configurations $\mu_1, \dots, \mu_N \in M$. Here, we focus on learnable solvers that employ neural networks, thus casting our problem in the general framework of Section 4.

We focus on developing physically consistent neural network surrogates that ensure conservation of linear and angular momentum, by leveraging the spanning tree solver presented in Section 3. Recall that this solver is a linear operator $S_I : U'_h \times R'_h \rightarrow \Sigma_h$ that behaves as a right-inverse of the constraint operator B , meaning that $BS_I f = f$ for all $f \in U'_h \times R'_h$.

Due to its efficiency, the spanning tree solver can readily be integrated within the computational pipeline of reduced order models without degrading their overall performance. This gives us two main advantages. First, as discussed in Section 3, we can focus our attention on the stress field, i.e. on the map $\mu \rightarrow \sigma_\mu$. Using (3.2), we can leverage S_I to post-process both the displacement u and rotation r from a given surrogate stress σ . Secondly, the operator S_I allows us to construct subspaces of the kernel of B . For that, we define the operator

$$S_0 := I - S_I B.$$

Now $S_0 : \Sigma_h \rightarrow \ker(B)$ because $BS_0 = B - IB = 0$.

We can use this operator in two ways: either to split the stress tensor into a homogeneous term with respect to B and a non-homogeneous remainder, or to construct a corrector operator. The two approaches naturally give rise to two different strategies for reduced order modeling which we detail in Sections 5.1 and 5.2, respectively. An overview is provided in Table 1.

Table 1: Overview of the approaches considered for the approximation of the stress variable, complemented with their ansatz and corresponding formula (2nd and 3rd column, respectively).

Non-linear regression	$\sigma_\mu \approx \tilde{\sigma}_\mu$	$= \Phi(\boldsymbol{\mu})$
Split	$\sigma_\mu \approx \tilde{\sigma}_\mu^0 + \sigma_\mu^f$	$= \Phi_0(\boldsymbol{\mu}) + S_I f_\mu$
Corrected	$\sigma_\mu \approx \tilde{\sigma}_\mu^0 + \sigma_\mu^f$	$= V_0 V_0^\top (\tilde{\sigma}_\mu - \sigma_\mu^f) + \sigma_\mu^f$ $= V_0 V_0^\top (\Phi(\boldsymbol{\mu}) - S_I f_\mu) + S_I f_\mu$

5.1. The Split approach

Following the strategy from [5], we can exploit the operators S_0 and S_I to decompose the stress tensor into a *particular* solution, satisfying the conservation constraints, and a *homogeneous* solution, lying in the kernel of B . In particular,

$$\sigma = \underbrace{(\sigma - S_I f)}_{\in \ker(B)} + S_I f =: \sigma^0 + \sigma^f.$$

The key point here is that, in the parametric setting, the particular solution $\sigma^f = \sigma_\mu^f$ can be efficiently computed as

$$\sigma_\mu^f = S_I f_\mu,$$

In turn, we construct a neural network surrogate $\Phi_0 : M \rightarrow \ker(B)$ to approximate the homogeneous component, $\Phi_0(\boldsymbol{\mu}) \approx \sigma_\mu^0$, so that the stress approximation becomes:

$$\sigma_\mu^{\text{split}} := \Phi_0(\boldsymbol{\mu}) + S_I f_\mu.$$

The only caveat is to construct Φ_0 so that $\Phi_0(M) \subseteq \ker(B)$. Fortunately, this can be easily achieved via the POD-NN approach. As discussed in Remark 4.4, networks constructed using the POD-NN strategy are guaranteed to preserve *homogeneous* constraints, if the training set respects the homogeneous constraints.

In practice, we implement the *Split approach* as follows. First, we exploit the FOM to compute a random collection of PDE solutions, $\{(\boldsymbol{\mu}_i, \sigma_{\boldsymbol{\mu}_i})\}_{i=1}^N$, which we hereon refer to as training *snapshots*. Then, we leverage the operator S_0 to produce a training set of homogeneous solutions,

$$\{(\boldsymbol{\mu}_i, \sigma_{\boldsymbol{\mu}_i}^0)\}_{i=1}^N = \{(\boldsymbol{\mu}_i, S_0 \sigma_{\boldsymbol{\mu}_i})\}_{i=1}^N,$$

We then perform POD over these snapshots to produce a subspace $V_0 \subseteq \ker(B)$ of dimension n_{rb} . Finally, we introduce a latent neural network $\phi : M \rightarrow \mathbb{R}^{n_{rb}}$ and define Φ_0 as

$$\Phi_0(\boldsymbol{\mu}) = V_0 \phi_0(\boldsymbol{\mu}).$$

Then, up to identifying the vector representation with its corresponding function representation, we have $\Phi_0 : M \rightarrow V_0 \subseteq \ker(B)$, as desired.

5.2. The Corrected approach

A second strategy is to leverage the operators S_0 and S_I to construct a *corrector*. The idea is based on the following lemma.

Lemma 5.1. *Let $V_0 \subseteq S_0(\Sigma_h) = \ker B$ and let $\pi_0 : \Sigma_h \rightarrow V_0$ be the orthogonal projection onto V_0 in the ℓ^2 inner product. Define*

$$\epsilon := \sup_{\boldsymbol{\mu} \in M} \|(I - \pi_0)S_0\sigma_{\boldsymbol{\mu}}\|,$$

where $\sigma_{\boldsymbol{\mu}} \in \Sigma_h$ is the FOM solution from (5.1), and $\|\cdot\|$ is the ℓ^2 -norm. Let the correction map $C : \Sigma_h \times M \rightarrow \Sigma_h$ be given by

$$C(\tilde{\sigma}, \boldsymbol{\mu}) := \pi_0(\tilde{\sigma} - S_I f_{\boldsymbol{\mu}}) + S_I f_{\boldsymbol{\mu}}.$$

Then, for all $\tilde{\sigma} \in \Sigma_h$ and all $\boldsymbol{\mu} \in M$ one has

- i) $BC(\tilde{\sigma}, \boldsymbol{\mu}) = f_{\boldsymbol{\mu}}$,
- ii) $\|\sigma_{\boldsymbol{\mu}} - C(\tilde{\sigma}, \boldsymbol{\mu})\| \leq \|\sigma_{\boldsymbol{\mu}} - \tilde{\sigma}\| + \epsilon$.

Proof. i) follows from the fact that $B\pi_0 \equiv 0$ and thus $BC(\tilde{\sigma}, \boldsymbol{\mu}) = BS_I f_{\boldsymbol{\mu}} = f_{\boldsymbol{\mu}}$. For ii), we let $\sigma_{\boldsymbol{\mu}}^0 := S_0\sigma_{\boldsymbol{\mu}} = \sigma_{\boldsymbol{\mu}} - S_I f_{\boldsymbol{\mu}}$. The orthogonality of π_0 then allows us to derive

$$\begin{aligned} \|\sigma_{\boldsymbol{\mu}} - C(\tilde{\sigma}, \boldsymbol{\mu})\|^2 &= \|\sigma_{\boldsymbol{\mu}}^0 + S_I f_{\boldsymbol{\mu}} - C(\tilde{\sigma}, \boldsymbol{\mu})\|^2 \\ &= \|\sigma_{\boldsymbol{\mu}}^0 - \pi_0(\tilde{\sigma} - S_I f_{\boldsymbol{\mu}})\|^2 \\ &= \|\sigma_{\boldsymbol{\mu}}^0 - \pi_0(\sigma_{\boldsymbol{\mu}}^0)\|^2 + \|\pi_0(\sigma_{\boldsymbol{\mu}}^0) - \pi_0(\tilde{\sigma} - S_I f_{\boldsymbol{\mu}})\|^2 \\ &\leq \epsilon^2 + \|\sigma_{\boldsymbol{\mu}}^0 - \tilde{\sigma} + S_I f_{\boldsymbol{\mu}}\|^2 \\ &= \epsilon^2 + \|\sigma_{\boldsymbol{\mu}} - \tilde{\sigma}\|^2. \end{aligned}$$

Since $\sqrt{a+b} \leq \sqrt{a} + \sqrt{b}$, the conclusion follows. \square

Remark 5.2. *Lemma 5.1 can easily be adapted to a different norm, including $\|\cdot\|_{\Sigma_h}$ from (2.6).*

The operator C in Lemma 5.1 acts as a corrector in the sense that, given $\boldsymbol{\mu} \in M$ and any $\tilde{\sigma} \in \Sigma_h$: it forces $C(\tilde{\sigma}, \boldsymbol{\mu})$ to satisfy the linear constraint associated to $\boldsymbol{\mu}$ while simultaneously bringing $\tilde{\sigma}$ towards $\sigma_{\boldsymbol{\mu}}$: see (i) and (ii), respectively. We emphasize that the subspace $V_0 \subseteq \ker B$ needs to be chosen properly, so that ϵ is sufficiently small. In practice, this can be achieved as in Section 5.1, by extracting a POD basis from a set of homogeneous snapshots $\{S_0\sigma_{\boldsymbol{\mu}_i}\}_{i=1}^N$.

We now have the ingredients necessary to construct the *Corrected approach*. Given a dataset $\{\boldsymbol{\mu}_i, \sigma_{\boldsymbol{\mu}_i}\}_{i=1}^N \subseteq M \times \Sigma_h$, we first train a classical neural network model Φ such that $\Phi(\boldsymbol{\mu}) \approx \sigma_{\boldsymbol{\mu}}$. Then, we exploit the dataset and the operator S_0 to construct a subspace $V_0 \subseteq \ker B$ of which we compute the corresponding projection π_0 . Then, following Lemma 5.1, we set

$$\sigma_{\boldsymbol{\mu}}^{\text{cor}} := \pi_0(\Phi(\boldsymbol{\mu}) - S_I f_{\boldsymbol{\mu}}) + S_I f_{\boldsymbol{\mu}},$$

as our final approximation for the stress field. Equivalently, using matrix-vector notation, $\sigma_{\boldsymbol{\mu}}^{\text{cor}} = V_0 V_0^\top (\Phi(\boldsymbol{\mu}) - S_I f_{\boldsymbol{\mu}}) + S_I f_{\boldsymbol{\mu}}$: see also Table 1.

Remark 5.3. *The Corrected approach follows a paradigm that is very close to the one adopted by the Split approach: the difference lies in how they approximate the homogeneous component of the stress field. It is worth mentioning that, from a practical point of view, this difference may*

prove significant. For instance, it has been observed that neural network models can efficiently approximate functions with small Lipschitz constant [15]. If we assume the parameter-to-solution map $\boldsymbol{\mu} \rightarrow \sigma_{\boldsymbol{\mu}}$ to be L -Lipschitz, then we may bound the Lipschitz constant of the homogeneous counterpart, $\boldsymbol{\mu} \rightarrow \sigma_{\boldsymbol{\mu}}^0$, as $\varrho_0 L$, where ϱ_0 denotes the spectral radius of S_0 . The Corrected approach and the Split approach then entail learning a map whose Lipschitz constant is L or $\varrho_0 L$, respectively. Consequently, if $\varrho_0 > 1$, we might expect the Corrected approach to perform better.

6. Numerical experiments

We devote this section to the empirical assessment of the proposed approaches. To this end, we consider three test cases of increasing complexity: a footing problem in 2D with four parameters (Section 6.1), a cantilever problem in 3D, featuring three parameters (Section 6.2), and a non-linear problem in 2D based on the Hencky-von Mises model, where four parameters describe the non-linear constitutive relations of the Lamé coefficients.

In order to verify the advantages of the proposed approaches over standard neural network regression, our analysis will include two benchmark models in which the stress tensor is approximated using a purely data-driven approach, $\sigma_{\boldsymbol{\mu}} \approx \Phi(\boldsymbol{\mu})$, whereas the displacement u and the rotation r are obtained via the post-processing of (3.2). Specifically, we consider the following benchmark models:

- *Black-box*. In this case, Φ is a classical feed forward neural network, designed and trained as in Section 4.1;
- *POD-NN*. In this case, the neural network model approximating the stress variable is constructed using the POD-NN strategy. We emphasize that, despite its black-box nature, this approach is consistent with the conservation of *angular* momentum (2.2c). This is because POD-based surrogates are known to preserve homogeneous constraints, as noted in Remark 4.4. On the other hand, there is no guarantee on the conservation of *linear* momentum.

To ensure a fair and systematic comparison, all approaches utilize neural networks with the same architecture, with structural changes only allowed between test cases. Details concerning the architecture are given in Appendix B. For each test case, we train the models on $N_{\text{train}} = 150$ randomly generated snapshots and assess their performance using an independent test set of $N_{\text{test}} = 50$ instances. Quantitatively, we measure the quality of the approximation using the Σ_h -mean relative error (Σ_h -MRE), computed as

$$\Sigma_h\text{-MRE} = \frac{1}{N_{\text{test}}} \sum_{i=1}^{N_{\text{test}}} \frac{\|\sigma_{\boldsymbol{\mu}_i^{\text{test}}} - \tilde{\sigma}_{\boldsymbol{\mu}_i^{\text{test}}}\|_{\Sigma_h}}{\|\sigma_{\boldsymbol{\mu}_i^{\text{test}}}\|_{\Sigma_h}}. \quad (6.1)$$

We use analogous metrics for the displacement u and the rotation r , respectively denoted as U_h -MRE and R_h -MRE, cf. Eq. (2.6). Here, $\{\boldsymbol{\mu}_i^{\text{test}}\}_{i=1}^{N_{\text{test}}}$ are the parameter instances in the test set, whereas $\sigma_{\boldsymbol{\mu}_i^{\text{test}}}$ and $\tilde{\sigma}_{\boldsymbol{\mu}_i^{\text{test}}}$ are the FOM reference and the ROM approximation, respectively.

To evaluate the fulfillment of the conservation laws, we also compute the average constraint violation (ACV), given by

$$\text{ACV} = \frac{1}{N_{\text{test}}} \sum_{i=1}^{N_{\text{test}}} \|B\tilde{\sigma}_{\boldsymbol{\mu}_i^{\text{test}}} - f_{\boldsymbol{\mu}_i^{\text{test}}}\|_{\ell^\infty}. \quad (6.2)$$

All test cases were coded in Python 3 using the libraries PorePy [19], PyGeoN [7], DL-ROMs [12], and a dedicated module available at github.com/compgeo-mox/conservative_ml_elasticity. All computational grids are made of shape-regular simplices, generated by Gmsh [14].

6.1. Linearized elasticity in 2D

In this first test case, we consider the classical footing problem with a body force in two dimensions. The domain Ω is given by the unit square. At the bottom boundary, a no-displacement condition is applied, $u = 0$, while homogeneous normal stress $\nu \cdot \sigma = 0$ is imposed on the left and right sides. On the top boundary, we impose a parameter dependent, downward force

$$g_u = 10^{-3} \cdot [0, -g_y]^\top \quad \text{with} \quad 0.5 \leq f_y \leq 2.$$

To make the constraint associated to the linear momentum equation more challenging, we consider a parametric body force equal to

$$f_u = 10^{-2} \cdot [0, -f_y]^\top \quad \text{with} \quad 0.5 \leq g_y \leq 2.$$

Finally, we set the parameter dependent Lamé coefficients in the ranges

$$0 \leq \mu \leq 2 \quad \text{and} \quad 0.1 \leq \lambda \leq 2.$$

The parameter space is thus four dimensional, with $\boldsymbol{\mu} = [g_y, f_y, \mu, \lambda]$. For the spatial discretization, we use a computational grid of 242 triangles with mesh size $h = 0.1$.

The results are presented in Table 2 and Figures 2 and 3. Overall, the approaches provide a satisfactory approximation of the stress field when evaluated using the Σ_h -metric. In particular, Table 2 shows that all methods report an average Σ_h error below 2%. However, these inaccuracies propagate to the variables u and r , with the rotation field being the most sensitive.

Notably, the approximations provided by the Black-box and POD-NN approaches show a significant disagreement with the conservation laws, with ACV values 9 orders of magnitude larger than those reported by our proposed approaches. In contrast, both the Split and the Corrected approach manage to fulfill the conservation constraints up to machine precision, as expected by the theory.

Table 2: Results for the case study in Section 6.1. We report the MREs for stress, σ , displacement, u , and rotation, r , for the three ROM approaches. Each MRE is computed according to the natural norm associated to the underlying finite element space, see, e.g., Eq. (6.1). The last column reports the average constraint violation ACV computed as in Eq. (6.2).

ROM	Σ_h -MRE [σ]	U_h -MRE [u]	R_h -MRE [r]	ACV
Black-box	9.86e-03	1.28e-02	1.32e-01	3.03e-03
POD-NN	6.39e-03	9.12e-03	7.38e-02	3.30e-05
Corrected	5.96e-03	9.25e-03	7.34e-02	1.14e-14
Split	1.37e-02	7.76e-02	7.34e-01	1.13e-14

As seen in Figure 2, these consideration not only hold in the average sense, but also from a global perspective. There, we can also appreciate that the POD-NN and the Corrected approaches produce comparable error distributions, while the Split and Black-box methods show a less favorable performance. To summarize, the Corrected approach shows the best performance for this case, as it manages to ensure physical consistency while also achieving state-of-the-art performance with respect to Σ_h and L^2 metrics.

The Split approach, instead, guarantees momentum conservation but produces larger errors, which result in a poor approximation of the displacement u and the rotation r . A visual

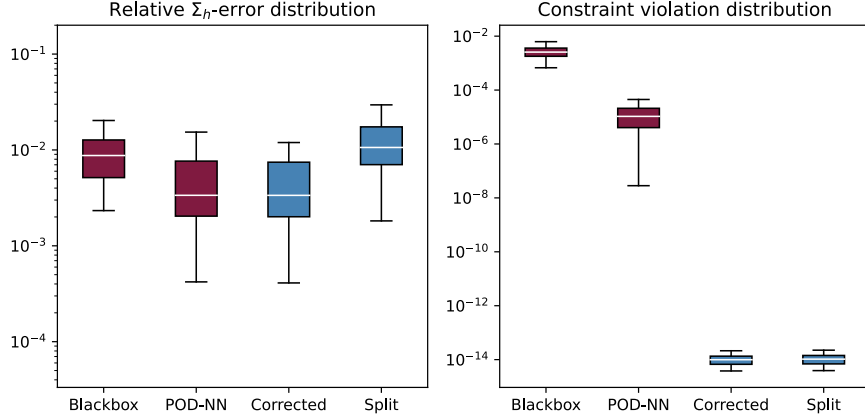


Figure 2: Errors distribution in the stress variable for the case study of Section 6.1. Σ_h -relative errors (left) are obtained by the summands in (6.1). Similarly, measurements for the constraint violation (right) refer to (6.2).

inspection of the displacement fields, cf. Figure 3, highlights this phenomenon. While the approximation produced by the Corrected approach is satisfactory, we notice that the Split approach produces some geometrical artifacts that seem related to the structure of the spanning tree solver.

6.2. Linearized elasticity in 3D

As our second test case, we consider a cantilever fixed at one end and subjected to a body force. The computational domain is given by $\Omega = (0, 2) \times (0, 0.5) \times (0, 0.5)$. On the left side, i.e. for $x = 0$, we set $u = 0$, while on the remaining boundary we impose zero traction, $\nu \cdot \sigma = 0$. The body force is parametric and given by

$$f_u = 10^{-2} \cdot [0, 0, -f_z]^\top \quad \text{with} \quad 0.5 \leq f_z \leq 2.$$

In this case, the Lamé coefficients are parametrized as

$$0 \leq \mu \leq 2 \quad \text{and} \quad 0.1 \leq \lambda \leq 2.$$

Consequently, this case study features three parameters, $\boldsymbol{\mu} = [f_z, \mu, \lambda]$. To construct the FOM we use a mesh of stepsize $h = 0.2$, resulting in a computational grid with 412 tetrahedra.

The numerical results are reported in Table 3 and Figures 4-5. As in the previous test case, we observe that in terms of Σ_h and L^2 accuracy, the Corrected approach performs comparably to both POD-NN and naive Black-box regression, while the Split algorithm produces errors that are an order of magnitude higher than the others. Again, the Corrected and the Split approaches fulfill the physical constraints exactly, by construction. In this respect, POD-NN performs slightly better than Black-box regression. Indeed, Figure 4 shows that POD-NN yields constraint residuals below 10^{-4} , whereas the Black-box performs poorly with a residual above 10^{-3} . This effect is most likely caused by the inherent ability of POD-NN to account for the conservation of angular momentum (cf. Remark 4.4). The conservation of linear momentum, however, is not guaranteed, resulting in an ACV of $1.82 \cdot 10^{-5}$ for POD-NN, as shown in Table 3.

We note that the error propagation during the post-processing of phase is milder in this case. In particular, we notice that all methods manage to produce reasonable approximations of the displacement field. In fact, the FOM and the ROM simulations are nearly indistinguishable in Figure 5.

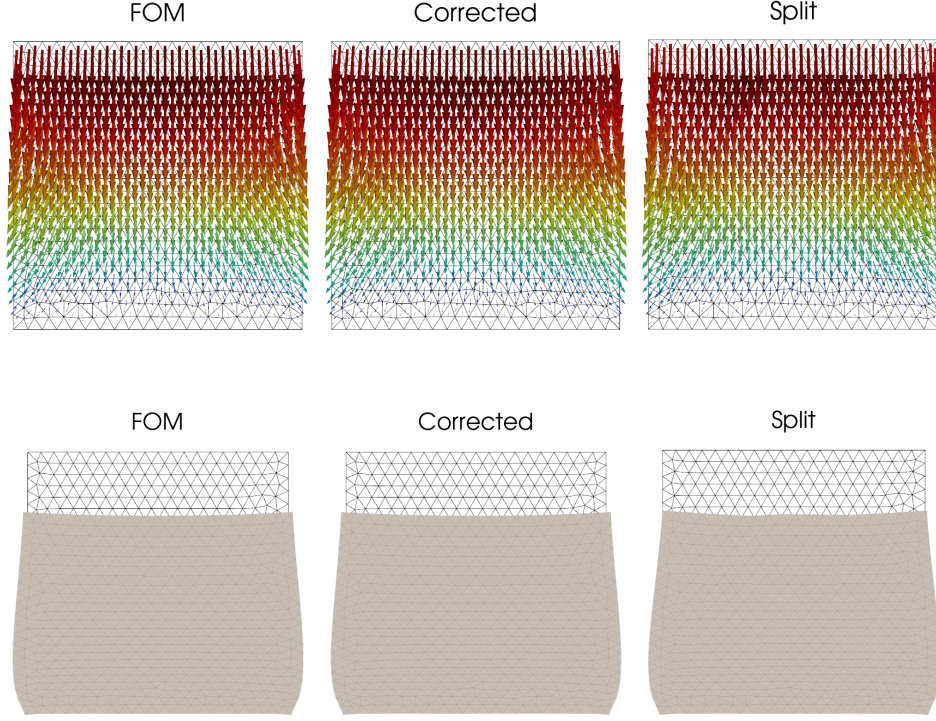


Figure 3: Comparison between FOM and conservative solvers for the footing problem of Section 6.1. Parameter values have been selected at random from the test set: $g_y = 1.167e-03$, $f_y = 7.800e-03$, $\mu = 1.055$, $\lambda = 1.593$. Top: quiver plots of the displacement field u . Bottom: original domain (grid) and exaggerated, deformed domain according to the computed displacement (grey; exaggeration factor: 150).

6.3. Non-linear elasticity in 2D

In this last test case, we consider a non-linear model of Hencky-von Mises type, cf. Example 2.2. Let $\Omega = (0,1)^2$ be the unit square, on which we generate a grid of 944 triangles with a mesh size of $h = 0.05$. We consider a parametrized variant of the model in [13], where the Lamé parameters depend on the norm of the deviatoric strain $\zeta = \|\text{dev } \varepsilon u\|$. Specifically, we consider the following expressions for μ and λ

$$\lambda(\zeta) := \alpha \left(1 - \frac{1}{2} \mu(\zeta) \right), \quad \mu(\zeta) := 1 + (1 + \zeta^2)^{\frac{\beta-2}{2}},$$

for given parameters $\alpha \geq 0$ and $\beta \leq 2$. Note that $1 \leq \mu(\zeta) \leq 2$ and $0 \leq \lambda(\zeta) \leq \alpha/2$, resulting in a physically relevant range for the Lamé parameters.

We impose the displacement as g_u on the entire boundary and include a body force f_u , given by

$$g_u(x, y) = \frac{\gamma}{10} \begin{bmatrix} x(1-x) \\ y(1-y) \end{bmatrix}, \quad f_u(x, y) = \delta \begin{bmatrix} (4y-1)(4y-3) \\ (4x-1)(4x-3) \end{bmatrix},$$

Table 3: Results for the test case in Section 6.2. Table entries read as in Table 2.

ROM	Σ_h -MRE [σ]	U_h -MRE [u]	R_h -MRE [r]	ACV
Black-box	6.09e-03	3.20e-03	3.30e-03	4.32e-03
POD-NN	5.17e-03	4.05e-03	4.05e-03	1.82e-05
Corrected	3.52e-03	3.21e-03	3.05e-03	1.64e-13
Split	1.49e-02	3.10e-02	2.84e-02	1.69e-13

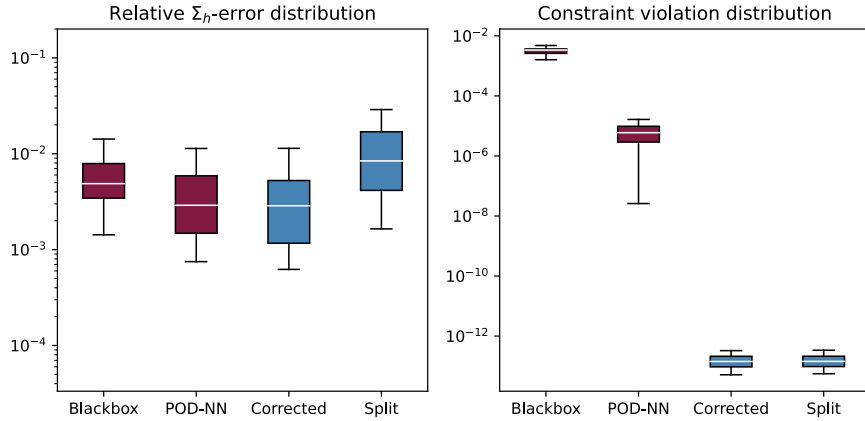


Figure 4: Σ_h -relative errors in the stress and constraint violation for the second test case, Section 6.2. Panels read as in Figure 2.

with γ and δ model parameters. We allow the four parameters $\boldsymbol{\mu} = [\alpha, \beta, \gamma, \delta]$ to attain values in the following ranges

$$1 \leq \alpha \leq 2, \quad 0 \leq \beta \leq 2, \quad -1 \leq \gamma \leq 1, \quad -1 \leq \delta \leq 1.$$

The numerical results are reported in Table 4 and Figures 6 and 7. Again, the Corrected approach outperforms both POD-NN and Black-box. The Split approach exhibits the worst performance in all metrics. Both benchmark models violate the physical constraints significantly, with ACV values above 10^{-3} , while the proposed approaches manage to conserve linear and angular momentum up to machine precision. As shown in Figure 6, these observations apply consistently across the entire parameter space.

Among classical methods, POD-NN is the better alternative, but it fails to provide physical consistency. Our proposed approaches, instead, are capable of guaranteeing momentum conservation, in line with Sections 6.1-6.2. However, only the Corrected method succeeds in doing so without introducing numerical artifacts. The Split approach, on the other hand, yields unsatisfactory results in all variables.

This is particularly evident in Figure 7, where we illustrate the deformed domain based on the computed displacements. While the Corrected solution is indistinguishable from the FOM, we observe large deviations for the Split approach, especially in the center of the domain. Once again, this suggests a high sensitivity of the Split approach with respect to the spanning tree, as alluded to in Remark 5.3. In this case, we used the multi-root spanning tree illustrated in Figure 1(right), which results in multiple independent trees reaching towards the center of Ω .

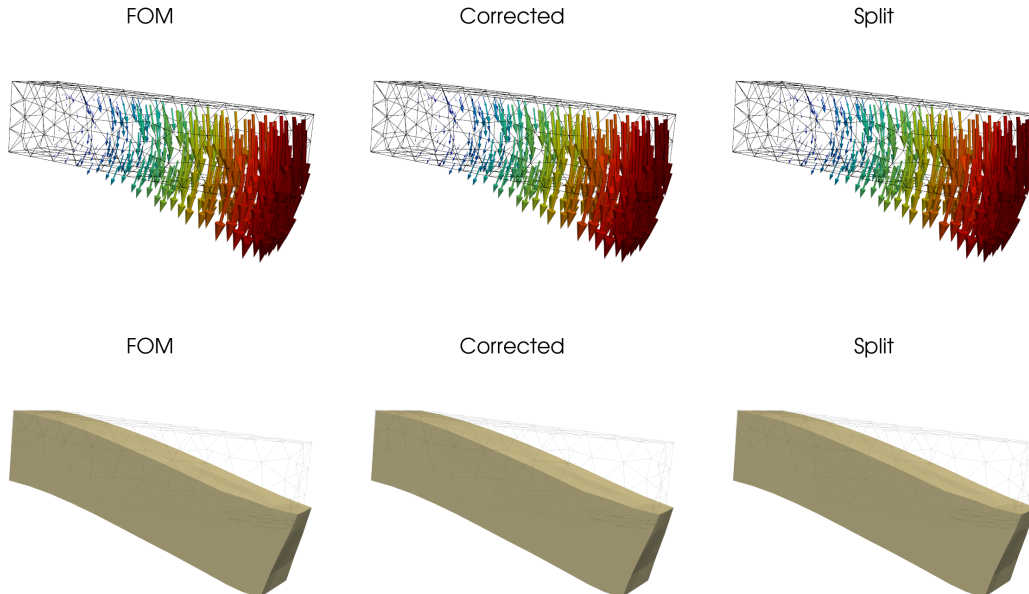


Figure 5: Comparison between FOM and conservative solvers for the cantilever problem of Section 6.2. Parameter values have been selected at random from the test set: $\mu = 1.826$, $\lambda = 0.590$, $f_z = 0.0182$. Top: quiver plots of the displacement field u . Bottom: original domain (grid) and corresponding deformed domain (grey). The quiver plots are directly generated in PyVista [27] using the displacement as cell data. The generation of warp plots, on the other hand, relies on an interpolation procedure (intrinsic to PyVista) which maps cell data to point data. This may generate visual artifacts when the mesh is coarse, as apparent at the right end of the domain.

This structure is clearly visible in the approximation proposed by the Split approach, suggesting a strong correlation between the two.

We conclude with a final observation concerning the computational cost¹. Due to the non-linear nature of the problem, each simulation of the FOM requires roughly 1 minute (see Table 5). Approximately 7 seconds are required for setting up the model, while solving the system takes ~ 54 seconds, for each parameter instance μ . The FOM produces the three fields (σ_h, u_h, r_h) simultaneously since the triplet is considered as a single unknown in the product space $\Sigma_h \times U_h \times R_h$.

In contrast, the proposed deep learning based ROMs are significantly faster, as shown in Table 5. Although the ROM requires the same amount of time to be initialized, roughly 7 seconds, generating solutions for the stress field only takes a few milliseconds. In particular, once the FOM and the ROM have been set up, the latter is $\times 6000$ faster in computing the stress field. However, the post-processing of the displacement u and rotation r requires an additional time of around ~ 11 seconds. This additional cost is due to the additional assembly of several operators at the FOM level for given σ_h . Nevertheless, this burden is mitigated by the efficiency of the spanning tree solver.

¹Clock times were recorded using a personal laptop: MSI Prestige 15 with an 11th-gen 3GHz Intel i7 processor, 16GB of RAM, and an NVIDIA GeForce GTX 1650 Max-Q GPU (4GB). Consequently, the reported values are inherently dependent on the specific hardware and implementation, but they still serve as a useful basis for performance comparison.

Table 4: Results for the test case in Section 6.3. Table entries read as in Table 2.

ROM	Σ_h -MRE [σ]	U_h -MRE [u]	R_h -MRE [r]	ACV
Black-box	6.23e-03	6.52e-03	6.18e-03	1.17e-02
POD-NN	7.46e-04	7.87e-04	8.86e-04	1.16e-03
Corrected	5.91e-04	7.07e-04	7.42e-04	1.37e-13
Split	3.83e-03	1.06e-01	1.62e-01	1.39e-13

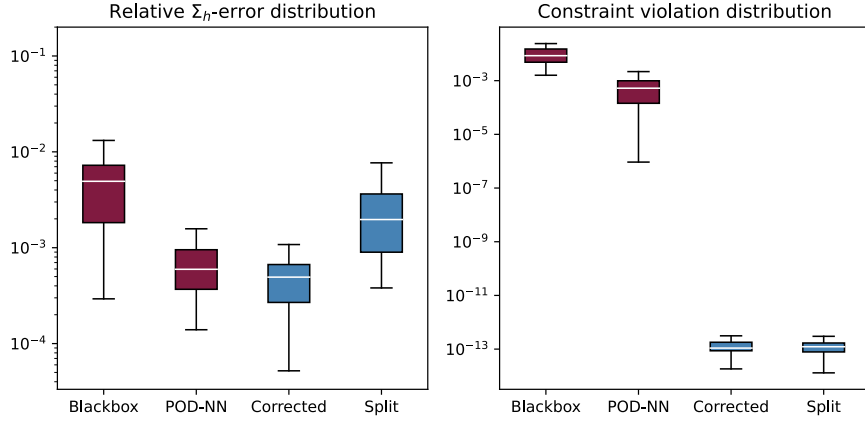


Figure 6: Σ_h -relative errors for the stress and constraint violation for the test case of Section 6.3. Panels read as in Figure 2.

Table 5: Comparison of computational times for the Hencky-von Mises problem of Section 6.3. Results limited to the best ROM according to Table 4. Setup time refers to the time required to initialize the solver (thus not affecting subsequent queries). Computing σ is the time required to compute the stress field. Getting (u, r) refers to the time needed to produce a full solution.

	Setup time	Computing σ	Computing (u, r)
FOM	6.95 s	54.62 s	0 s
ROM (Corrected)	7.32 s	0.0089 s	11.46 s

Thus, the proposed ROM can provide varying levels of speed-up, depending on whether the entire solution is required or if only the stress field is needed. Specifically, for applications where determining the stress field σ is of interest, e.g. in evaluating fault stability or assessing structural integrity of the medium, our proposed approach provides an attractive advantage.

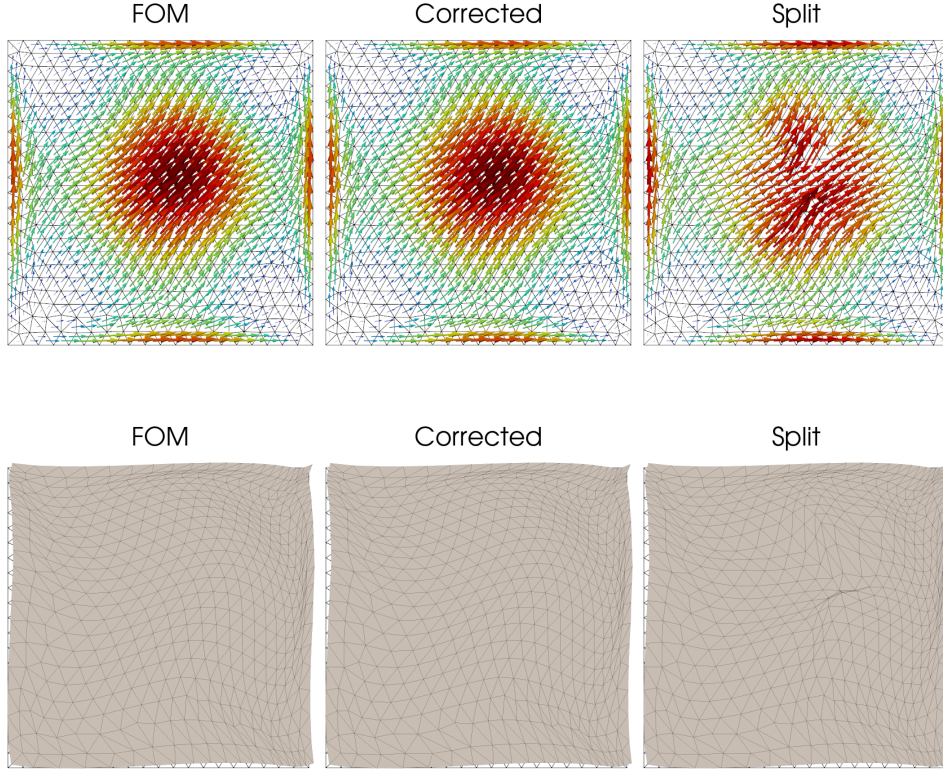


Figure 7: Comparison between FOM and conservative solvers for the Hencky-von Mises model of Section 6.3. Parameter values have been selected at random from the test set: $\alpha = 1.311$, $\beta = 1.601$, $\gamma = 0.540$, $\delta = -0.646$. Top: quiver plots of the displacement field u . Bottom: the deformed domain (exaggeration factor: 20).

7. Conclusions

In this work, we have introduced two new reduced order models for elasticity problems that guarantee conservation of linear and angular momentum. The analysis was conducted within the context of data-driven ROMs, where, for problems of this type, methods such as POD-NN constitute the state-of-the-art. Therefore, our effort can be understood as an attempt to bring data-driven surrogates closer to classical physics-based ROMs, such as POD-Galerkin and other Reduced Basis methods.

These two approaches are based on a suitable decomposition of the stress into an homogeneous and a particular parts, where the latter does not depend on the parameters and is the same for both approaches. The actual construction of the homogeneous solution is method specific. The computation of the particular solution is based on a spanning tree strategy to appropriately select suitable degrees of freedom, in order to obtain a (block) triangular system and thus making the computation of the particular solution inexpensive. On the other side, the homogeneous solutions are built based on suitable trained reduced models. In the online phase, the resulting approaches are thus effective and computationally efficient in providing approximations of the stress field fulfilling the linear constraints exactly.

We assessed the capabilities of the proposed approaches by comparing their performances

against POD-NN (a state-of-the-art approach within the class of data-driven ROMs) and naive neural network regression, which, given our proposal, constitute a natural benchmark. The latter, in fact, can be very accurate when considering crude L^2 metrics², but they are not guaranteed to yield physical results.

All our numerical experiments suggest the same conclusion: while black-box methods based on neural networks can achieve small relative errors in the L^2 sense, their approximations consistently violate the momentum equations, with maximum cell-wise residuals in the order of $10^{-2} - 10^{-5}$. Our proposed approaches, instead, are always in exact agreement with the conservation laws, yielding cell-wise residuals close to machine precision. However, of the two proposed strategies (Corrected and Split), only the Corrected approach managed to achieve this physical consistency while simultaneously delivering L^2 -accurate solutions, thus consistently outperforming all benchmark models. The Split method, on the other hand, was not as convincing: its approximations of the stress field were often affected by numerical artifacts and, during the post-processing phase, these inaccuracies tended to propagate over both the displacement u and the rotation r .

In conclusion, we presented two possible approaches for the construction of physically consistent neural network solvers compatible, one of which was capable of achieving state-of-the-art performance while ensuring the conservation of both linear and angular momentum. The approach also showed remarkable speed ups with respect to the FOM, especially for what concerns the computation of the stress field. This can be particularly interesting for applications in geomechanics and civil engineering involving, for instance, the evaluation of structural integrity, fault stability or crack propagation.

Future works could be devoted to further improving the computational speed up as to ensure that the efficiency in computing the stress field can directly transfer to the displacement u and the rotation r as well.

A. Principal Orthogonal Decomposition (POD)

Let $\{\xi_i\}_{i=1}^N \subset H$ be a point cloud in \mathbb{R}^{N_h} . Proper Orthogonal Decomposition is an algorithm that, given a reduced dimension $n \ll \min\{N, N_h\}$, seeks for the matrix $V_n \in \mathbb{R}^{N_h \times n}$ that minimizes the mean squared projection error, i.e.

$$V_n := \operatorname{argmin}_{W \in \mathbb{R}^{N_h \times n}} \frac{1}{N} \sum_{i=1}^N \|\xi_i - WW^\top \xi_i\|^2. \quad (\text{A.1})$$

The solution to the latter minimization problem is known in closed form and it can be computed via truncated Singular Value Decomposition (SVD). More precisely, let

$$\Xi := [\xi_1, \dots, \xi_N] \in \mathbb{R}^{N_h \times N},$$

be the so-called snapshots matrix. Computing an SVD of the above yields

$$\Xi = V \Sigma U^\top,$$

for suitable orthonormal matrices $U, V \in \mathbb{R}^{N \times r}$, and a diagonal matrix $\Sigma \in \mathbb{R}^{r \times r}$. Without loss of generality, we assume the entries $\Sigma = \operatorname{diag}(s_1, \dots, s_r)$ to be sorted such that $s_1 \geq \dots \geq s_r \geq 0$. Here, $r := \operatorname{rank}(\Xi)$.

²Recall that $\|\sigma\|_{L^2(\Omega)} \leq \|\sigma\|_{\Sigma_h}$ and $\|u\|_{U_h} = \|u\|_{L^2(\Omega)}$, $\|r\|_{R_h} = \|r\|_{L^2(\Omega)}$.

Then, the POD algorithm finds \mathbf{V}_n by extracting the submatrix corresponding to the first n columns of \mathbf{V} . It can be proven that this procedure actually results in a solution to (A.1): see, e.g., [24, Proposition 6.1]. We mention that, given any positive definite matrix $\mathbf{G} \in \mathbb{R}^{N_h \times N_h}$, one can replace the ℓ^2 -norm in (A.1) with the weighted norm $\|\cdot\|_{\mathbf{G}}$ induced by the inner-product,

$$\langle \xi, \eta \rangle_{\mathbf{G}} := \xi^\top \mathbf{G} \eta.$$

In practice, this boils down to computing an SVD of $\mathbf{G}^{1/2} \Xi$ and re-adapting the previous ideas: cf. [24, Proposition 6.2].

In both cases, the purpose of the POD is to construct a matrix spanning a subspace of dimension n that approximates the point cloud as accurately as possible. In fact, notice that for every ξ_i in the point cloud, due optimality of orthogonal projections,

$$\|\xi_i - \mathbf{V}_n \mathbf{V}_n^\top \xi_i\|^2 = \min_{\eta \in \text{span}(\mathbf{V}_n)} \|\xi_i - \eta\|^2.$$

B. Neural network architectures

In this appendix, we provide additional details on the neural network architectures implemented for the case studies in Section 6. In what follows, given two positive integers $p, k \in \mathbb{N}_+$, we denote by $F_{p,k}$ the map from $\mathbb{R}^p \rightarrow \mathbb{R}^{2pk+p}$ acting as

$$F_{p,k} : \begin{bmatrix} x_1 \\ x_2 \\ \vdots \\ x_p \end{bmatrix} \mapsto \begin{bmatrix} x_1 \\ \cos(x_1) \\ \sin(x_1) \\ \vdots \\ \cos(kx_1) \\ \sin(kx_1) \end{bmatrix} \oplus \begin{bmatrix} x_2 \\ \cos(x_2) \\ \sin(x_2) \\ \vdots \\ \cos(kx_2) \\ \sin(kx_2) \end{bmatrix} \oplus \dots \oplus \begin{bmatrix} x_p \\ \cos(x_p) \\ \sin(x_p) \\ \vdots \\ \cos(kx_p) \\ \sin(kx_p) \end{bmatrix}.$$

where \oplus is the concatenation operator, acting on pair of vectors $\mathbf{y} = [y_1, \dots, y_a]^\top$, $\mathbf{z} = [y_1, \dots, y_b]^\top$ as $\mathbf{y} \oplus \mathbf{z} := [y_1, \dots, y_a, z_1, \dots, z_b]^\top$. Essentially, $F_{p,k}$ acts as a feature augmentation map, adding sinusoidal transformations of each x_i up to frequency k . These maps are commonly used in the Deep Learning literature as a form of pre-processing and are sometimes referred to as *Fourier layers* (not to be confused with Fourier layers in Neural Operators [20], nor with classical dense layers: the ones discussed here, in fact, are *nontrainable*, as their definition does not include learnable parameters).

Conversely, following Definition 4.1, we denote by $D_{a,b}^\rho$ a generic dense feed forward layer from $\mathbb{R}^a \rightarrow \mathbb{R}^b$ with 0.1-leakyReLU activation, that is, relying upon

$$\rho(x) := \begin{cases} x & x \geq 0, \\ 0.1x & x < 0. \end{cases}$$

We also use the notation $D_{a,b}$, without superscript, to intend layers without activation.

With these convention, the architectures employed for the three case studies can be summarized with following scheme, shared by all models:

$$D_{N_h, n} \circ D_{n, 30}^\rho \circ D_{30, 30}^\rho \circ D_{30, 2pk+p} \circ F_{k, p}, \quad (\text{B.1})$$

where the only problem-dependent quantities are: p the number of PDE parameters, N_h the total number of dof in the stress field discretization, n and k . The values of these quantities are summarized in Table B.6.

More precisely, all models in Section 6 referred to as "Black-box" implement the architecture in Eq. (B.1). All the other approaches (POD-NN, Split, Corrected), instead, implement (B.1) using the POD-NN strategy. In particular, the terminal layer $D_{N_h, n}$ is replaced by the POD matrix $\mathbf{V} \in \mathbb{R}^{N_h \times n}$, acting linearly, and the activation of the second-last layer is removed, formally replacing $D_{n, 30}^\rho$ with $D_{n, 30}$. Consequently, for these architectures, n can be interpreted as the POD dimension (or, equivalently, the number of POD modes).

Table B.6: Number of parameters, p , number of dof, $N_h = \dim(\Sigma_h)$, POD dimension, n , and Fourier frequency, k , across the three case studies in Section 6.

Case study	p	N_h	n	k
§6.1 Footing problem	4	5824	10	3
§6.2 Cantilever	3	9018	7	3
§6.3 Hencky-von Mises	4	5824	15	2

Acknowledgements

AF has been partially funded by the PRIN project "FREYA - Fault REactivation: a hYbrid numerical Approach" - SLG2RIST01. NF has been supported by project Cal.Hub.Ria (Piano Operativo Salute, traiettoria 4), funded by MSAL. AF and NF are both members of "Gruppo Nazionale per il Calcolo Scientifico" (GNCS). The present research is part of the activities of "Dipartimento di Eccellenza 2023-2027", Italian Minister of University and Research (MUR), grant Dipartimento di Eccellenza 2023-2027.

References

- [1] D. ARNOLD, R. FALK, AND R. WINTHER, *Mixed finite element methods for linear elasticity with weakly imposed symmetry*, Mathematics of Computation, 76 (2007), pp. 1699–1723.
- [2] D. N. ARNOLD, R. S. FALK, AND R. WINTHER, *Finite element exterior calculus, homological techniques, and applications*, Acta numerica, 15 (2006), pp. 1–155.
- [3] T. BEUCLER, M. PRITCHARD, S. RASP, J. OTT, P. BALDI, AND P. GENTINE, *Enforcing analytic constraints in neural networks emulating physical systems*, Physical Review Letters, 126 (2021), p. 098302.
- [4] T. BOESEN, E. HABER, AND U. M. ASCHER, *Neural DAEs: Constrained neural networks*, arXiv preprint arXiv:2211.14302, (2022).
- [5] W. M. BOON, N. R. FRANCO, A. FUMAGALLI, AND P. ZUNINO, *Deep learning based reduced order modeling of Darcy flow systems with local mass conservation*, arXiv preprint arXiv:2311.14554, (2023).

- [6] W. M. BOON AND A. FUMAGALLI, *A reduced basis method for darcy flow systems that ensures local mass conservation by using exact discrete complexes*, Journal of Scientific Computing, 94 (2023).
- [7] W. M. BOON AND A. FUMAGALLI, *PyGeoN: a Python package for Geo-Numerics*, 2024. 10.5281/zenodo.13902300.
- [8] S. CUOMO, V. S. DI COLA, F. GIAMPAOLO, G. ROZZA, M. RAISSI, AND F. PICCIALI, *Scientific machine learning through physics-informed neural networks: Where we are and what's next*, Journal of Scientific Computing, 92 (2022), p. 88.
- [9] L. B. DA VEIGA, C. LOVADINA, AND D. MORA, *A virtual element method for elastic and inelastic problems on polytope meshes*, Computer methods in applied mechanics and engineering, 295 (2015), pp. 327–346.
- [10] E. DE LOS SANTOS, A. M. ALONSO RODRIGUEZ, AND F. RAPETTI, *Construction of a spanning tree for high-order edge elements*, International Journal of Numerical Modelling: Electronic Networks, Devices and Fields, 36 (2023), p. e3080.
- [11] N. FRANCO, A. MANZONI, AND P. ZUNINO, *A deep learning approach to reduced order modelling of parameter dependent partial differential equations*, Mathematics of Computation, 92 (2023), pp. 483–524.
- [12] N. R. FRANCO, *Nicolarfranco/dlroms: First release*, Aug. 2024. 10.5281/zenodo.13254758.
- [13] G. N. GATICA, A. MÁRQUEZ, AND W. RUDOLPH, *A priori and a posteriori error analyses of augmented twofold saddle point formulations for nonlinear elasticity problems*, Computer Methods in Applied Mechanics and Engineering, 264 (2013), pp. 23–48.
- [14] C. GEUZAIN AND J.-F. REMACLE, *Gmsh: A 3-d finite element mesh generator with built-in pre- and post-processing facilities*, International Journal for Numerical Methods in Engineering, 79 (2009), pp. 1309–1331.
- [15] I. GÜHRING AND M. RASLAN, *Approximation rates for neural networks with encodable weights in smoothness spaces*, Neural Networks, 134 (2021), pp. 107–130.
- [16] D. HANSEN, D. M. ROBINSON, S. ALIZADEH, G. GUPTA, AND M. MAHONEY, *Learning physical models that can respect conservation laws*, in Proceedings of the 40th International Conference on Machine Learning (ICML 2023), 2023, pp. 12469–12510.
- [17] J. S. HESTHAVEN, C. PAGLIANTINI, AND G. ROZZA, *Reduced basis methods for time-dependent problems*, Acta Numerica, 31 (2022), p. 265–345.
- [18] J. S. HESTHAVEN AND S. UBBIALI, *Non-intrusive reduced order modeling of nonlinear problems using neural networks*, Journal of Computational Physics, 363 (2018), pp. 55–78.
- [19] E. KEILEGAVLEN, R. BERGE, A. FUMAGALLI, M. STARNONI, I. STEFANSSON, J. VARELA, AND I. BERRE, *Porepy: An open-source software for simulation of multiphysics processes in fractured porous media*, Computational Geosciences, (2020).
- [20] N. KOVACHKI, Z. LI, B. LIU, K. AZIZZADENESHELI, K. BHATTACHARYA, A. STUART, AND A. ANANDKUMAR, *Neural operator: Learning maps between function spaces with applications to pdes*, Journal of Machine Learning Research, 24 (2023), pp. 1–97.

- [21] G. KUTYNIOK, P. PETERSEN, M. RASLAN, AND R. SCHNEIDER, *A theoretical analysis of deep neural networks and parametric pdes*, *Constructive Approximation*, 55 (2022), pp. 73–125.
- [22] S. LANTHALER, *Operator learning with pca-net: upper and lower complexity bounds*, *Journal of Machine Learning Research*, 24 (2023), pp. 1–67.
- [23] L. LU, X. MENG, S. CAI, Z. MAO, S. GOSWAMI, Z. ZHANG, AND G. E. KARNIADAKIS, *A comprehensive and fair comparison of two neural operators (with practical extensions) based on fair data*, *Computer Methods in Applied Mechanics and Engineering*, 393 (2022), p. 114778.
- [24] A. QUARTERONI, A. MANZONI, AND F. NEGRI, *Reduced Basis Methods for Partial Differential Equations: An Introduction*, Springer International Publishing, 2016.
- [25] M. RAISSI, P. PERDIKARIS, AND G. KARNIADAKIS, *Physics-informed neural networks: A deep learning framework for solving forward and inverse problems involving nonlinear partial differential equations*, *Journal of Computational Physics*, 378 (2019), p. 686 – 707.
- [26] L. RUTHOTTO AND E. HABER, *Deep neural networks motivated by partial differential equations*, *Journal of Mathematical Imaging and Vision*, 62 (2020), pp. 352–364.
- [27] C. B. SULLIVAN AND A. KASZYNSKI, *PyVista: 3d plotting and mesh analysis through a streamlined interface for the visualization toolkit (VTK)*, *Journal of Open Source Software*, 4 (2019), p. 1450.
- [28] N. TRASK, A. HUANG, AND X. HU, *Enforcing exact physics in scientific machine learning: a data-driven exterior calculus on graphs*, *Journal of Computational Physics*, 456 (2022), p. 110969.